ROYAL SOCIETY
OF CHEMISTRY

**PAPER**
Ganapathy Veerappan *et al.*
Low-temperature curable TiO₂ sol for separator and
HTM-free carbon-based perovskite solar cells

## PAPER

Check for updates

# Low-temperature curable TiO₂ sol for separator and HTM-free carbon-based perovskite solar cells†

Reshma Dileep K,[ab] Thulasi Raman Elumalai,[a] Easwaramoorthi Ramasamy, [iD][a] S. Mallick,[b] T. N. Rao[a] and Ganapathy Veerappan [iD] *[a]

In this study, we present the development of an ambient temperature curable TiO₂ mesoporous layer for perovskite solar cells (PSCs), eliminating the need for a binder and enabling the use of environmentally friendly solvents. The TiO₂ layer was synthesized *via* a hydrothermal method followed by minimal post-processing techniques. The resulting anatase TiO₂ sol was optimized to be compatible with various coating techniques such as spin coating, dip coating, and spray coating, allowing for its application at sub-50 °C temperatures. A comprehensive investigation was conducted to study the effects of annealing temperatures ranging from 50 °C to 500 °C on the crystallographic, morphological, electrical, and surface properties of the TiO₂ films derived from the TiO₂ sol. Contact angle measurements were employed to analyse the change in surface energy resulting from different sintering temperatures and its influence on the growth of the perovskite film on the TiO₂ films. To evaluate the performance of the TiO₂ electron transport layers (ETLs) annealed at different temperatures, carbon-based perovskite solar cells (CPSCs) were fabricated. The results revealed that the CPSCs utilizing the TiO₂ ETL annealed at 50 °C exhibited the highest efficiency of 11.1%, accompanied by an open circuit voltage of 0.98 V and a current density of 22.3 mA cm⁻². Notably, the developed TiO₂ ETL outperformed the commercial TiO₂ ETL sintered at 500 °C in the same device architecture. These findings demonstrate the potential of the ambient temperature curable TiO₂ ETL for large-area deposition and flexible PSCs.

## Introduction

The use of renewable energy resources is shifting to high gears as a result of the depleting non-renewable resources. The Sun is the most extensively harnessed renewable energy source, in the form of solar photovoltaic and solar thermal energy. Among various photovoltaic technologies, perovskite solar cells (PSCs) have proved to be promising due to their high power conversion efficiencies (PCEs), low-cost, and facile fabrication techniques. Perovskite absorbers are of high interest due to their outstanding intrinsic properties, such as tunable band gap over a large range, high absorption coefficient, long diffusion length, ambipolar charge transport, *etc.*[1] For photovoltaic applications, perovskite material (MaPbI₃) was first used in

2009 to replace the absorber material in a dye sensitized solar cell, and an efficiency of 3.8% was reported.[2] Though the PSCs were short-lived, this paved the way for a new class of solar cells. Various research groups carried out intense optimization around the world in material engineering, interface engineering, device architecture, optimization of various device fabrication steps, *etc.*,[3] which rendered an unprecedented improvement in the stability and photovoltaic performance of the PSCs.

Carbon based HTM-free PSCs (CPSCs) are one of the successful device architectures that circumvent the stability aspect as well as the cost of fabrication in a conventional PSC. CPSCs generally use the triple mesoscopic architecture (TiO₂/ZrO₂/perovskite/carbon), where TiO₂ is the electron transport layer (m-TiO₂), and mesoporous ZrO₂ or Al₂O₃ is used as the separator layer, with a carbon cathode.[4] The m-TiO₂ and the ZrO₂ layers require high temperature sintering, which increases the energy payback time, rendering the device fabrication process extensive and also limiting the usage of flexible polymer substrates. Another challenge in triple mesoscopic CPSCs is the perovskite infiltration, where the pore filling of the

[a] *Center for Solar Energy Materials, International Advanced Research Center for Powder Metallurgy and New Materials (ARCI), Balapur PO, Hyderabad 500005, Telangana, India. E-mail: ganagv@arci.res.in*

[b] *Department of Metallurgical Engineering & Materials Science, Indian Institute of Technology, Bombay, Powai, Mumbai 400076, Maharashtra, India*

perovskite is a major limiting factor in the performance of the CPSCs.[5] The ETL also plays a prominent role in dictating the performance of the CPSCs. The ETL facilitates the transport of the photogenerated electrons from the perovskite layer to the cathode. The conduction band edge conductivity, defects, lattice mismatch, *etc.*,[6] present in the ETL impact the photovoltaic performance and stability of PSCs. In the n–i–p device architecture, the perovskite layer is coated on the ETL; hence

the quality of the perovskite film and the growth characteristics often depend upon the quality of the underlying ETL. Various n-type semiconductor materials such as $TiO_2$, $SnO_2$, $ZnO$, $BaSnO_3$, $SrTiO_3$, *etc.*,[7] have been used as an ETL in PSCs and the widely explored one is $TiO_2$. CPSCs have explored m-$TiO_2$, which is processed at temperatures $> 450\ ^\circ C$. $SnO_2$ and $ZnO$ are the most commonly used low temperature processed ETLs in CPSCs.[5,8,9] For low temperature curable $TiO_2$ ETL development,
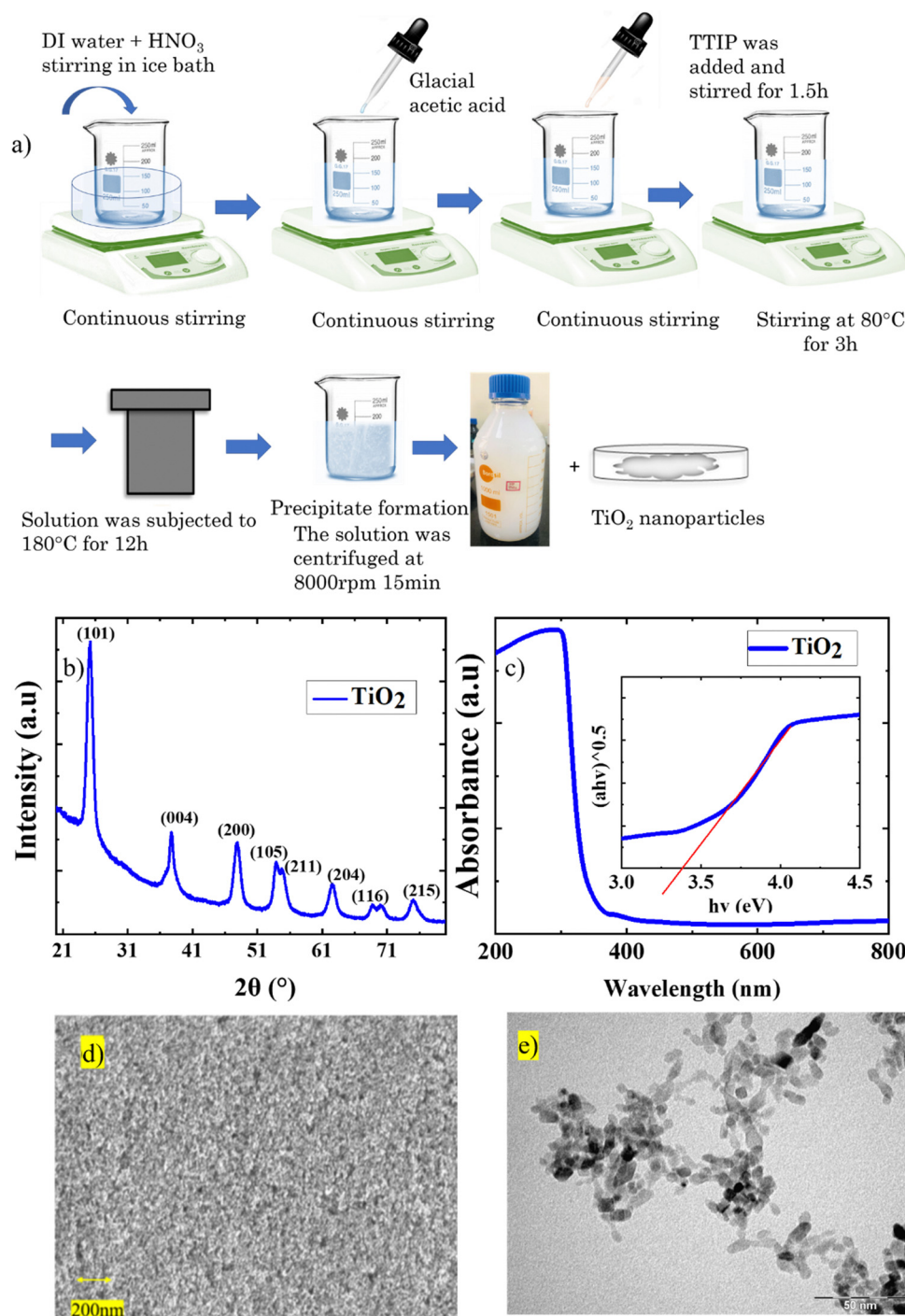


**Fig. 1** (a) Schematic representation of uniformly dispersed anatase $TiO_2$ sol and nanoparticle synthesis, (b) XRD spectra, (c) absorbance spectra (d) FE-SEM images and (e) TEM of $TiO_2$ films fabricated from $TiO_2$ sol.

vacuum-based deposition techniques such as atomic layer deposition,[10] electron-beam evaporation,[11] and magnetron sputtering[12] are used. UV curing was also explored as a route to reduce the annealing temperature of m-TiO$_2$.[13] However, solution-based techniques are more cost-effective and scalable. Coning et al. developed a transparent, stable TiO$_2$ dispersion that can be directly used without further processing where titanium diisopropoxide bis(acetylacetonate) was added to act as an electronic glue.[14] The compact TiO$_2$ layer processed by this method required low temperature annealing (150 °C).[14] In 2015, Di Li et al. developed an annealing free TiO$_2$ film for an electron collection layer in organic solar cells.[15] TiO$_2$ nanoparticles were synthesized via a hydrothermal method, and the nano particles were filtered out and then redispersed into solvents to obtain a colloidal solution of TiO$_2$.[15] Later in 2017, Yang et al. developed an annealing-free smooth anatase TiO$_2$ film with high optical transparency via a sol–gel method and successfully used it as a compact layer in PSCs.[16] Minghuang et al. used TiO$_2$ mesocrystals synthesized by a hydrothermal method and redispersed in ethanol, which was used as a mesoporous layer in PSC; the films were sintered at 150 °C for 30 min.[17] Though many solution processed low-temperature compact TiO$_2$ layers are used in PSCs, low-temperature m-TiO$_2$ films processed by a solution process are scarce.

Though various low temperature curable ETLs are used in CPSCs, solution processed ambient curable mesoporous TiO$_2$ is less explored.[18,19] In this regard, an ambient temperature curable anatase TiO$_2$ sol was developed in this work, which is highly stable, crystalline, and compatible with various deposition techniques such as dip coating, rod coating, slot-die coating and conventional deposition techniques (spin coating). The TiO$_2$ sol developed via hydrothermal synthesis with a yield > 60% constitutes green solvents such as water and ethanol and is devoid of organic binders and it can be generated in large volumes.

This work fabricated separator and HTM free-CPSCs with ambient temperature curable TiO$_2$ sol as the ETL, where MaPbI$_3$ is the absorber layer. Except for a single high temperature step used in device fabrication, all the other layers were processed at temperatures less than 100 °C, which is promising as it can reduce the energy payback period and simplify the fabrication steps. The ambient temperature processed TiO$_2$-based PSCs exhibited photovoltaic performance comparable to that of commercial TiO$_2$ (high temperature processing) with an open circuit voltage of > 1 V, which is higher than the commercial TiO$_2$ devices. The effect of sintering TiO$_2$ film at various temperatures on the photovoltaic performance was also evaluated. The PSCs with newly developed TiO$_2$ exhibited a power conversion efficiency of 11.1% with an open circuit voltage of 0.98 V and a short circuit current of 22.3 mA cm$^{-2}$.

## Experimental methods

### Synthesis of anatase TiO$_2$ sol

Anatase TiO$_2$ sol was synthesized via slight modifications in the synthesis procedure by Yang et al.[20] 120 mL of DI water was taken in a 250 mL beaker, into which 0.079 M of concentrated nitric acid was added. The beaker was set up in an ice bath and maintained under stirring. After cooling the solution to 0 °C, 0.347 M of glacial acetic acid and 0.341 M of titanium tetra isopropoxide (TTIP) were added dropwise into the solution under constant stirring and the solution was kept stirring for 1.5 h. The solution was heated to 80 °C and stirred for 3 h, after which it was cooled down to room temperature. The mixture was transferred into a Teflon lined autoclave and subjected to 180 °C for 12 h. The autoclave was cooled down to room temperature naturally. Then, the solution was divided into equal parts and centrifuged at 8000 rpm for 15 min several times. The supernatant was transferred into a separate container. The centrifugation was continued using ethanol and DI water. After each cleansing cycle, the supernatant was stored. This stored TiO$_2$ supernatant solution with DI water and ethanol constituted 500 mL.

## Results and discussion

Fig. 1(a) represents the schematic diagram of TiO$_2$ synthesis, and equation 1 gives the chemical reaction.

$$H_2O + HNO_3 + CH_3COOH + Ti(C_3H_7O)_4 = TiO_2 + (C_3H_8O)_4 + CH_3COONO_2 \tag{1}$$

TiO$_2$ nanoparticles are instantaneously formed on the addition of TTIP due to the hydrolysis of the precursors in the presence of HNO$_3$.[16] The rapid nucleation leads to the formation of stabilized TiO$_2$ nanoparticles. Subsequent aging at 80 °C triggers the formation of amorphous anatase TiO$_2$ particles within the stabilized nuclei.[16] The hydrothermal process utilizes high temperature (180 °C) and pressure aiding the formation of highly crystalline anatase TiO$_2$ nanoparticles.

The stability of the sol was analysed by measuring the zeta potential of the dispersion. The sol exhibited a zeta potential value of 49.9 mV, which is greater than 30 mV, and hence the particles are highly dispersed in the solution medium. This suggests that the sol is a highly stable, homogeneous dispersion of TiO$_2$ nanoparticles that can prevent the settling down of TiO$_2$ particles for an extended period.

Crystallographic studies of the TiO$_2$ film derived from the TiO$_2$ sol were carried out using XRD. The XRD spectrum (Fig. 1(b)) consists of major diffraction peaks at 25.5°, 37.7°, and 48.5°, which are in agreement with the anatase phase (JCPDS 02-0406).[20] The films formed are devoid of secondary phases and are highly crystalline in nature. The average crystallite size was calculated as 16.3 nm using the Scherrer equation. Fig. 1(c) represents the absorption spectra with Tauc's plot as an inset image and the yielded bandgap of 3.4 eV.

To gain further insight into the morphology and crystallographic features of the synthesized TiO$_2$ sol, FESEM, and TEM analysis were carried out. Fig. 1(d) shows the surface morphology image of the TiO$_2$ thin film. The films exhibit a uniformly distributed porous morphology. Fig. 1(e) represents

**Fig. 2** (a) XRD spectra and (b) absorption spectra with transmission spectra of 50 TiO$_2$, 100 TiO$_2$ and 500 TiO$_2$ as the inset image.

the TEM image, which depicts the elongated TiO$_2$ nanoparticles. As shown in Fig. S1(a) (ESI†), the sharp concentric circles from the SAED pattern were used to re-confirm the crystalline nature of the TiO$_2$. The concentric circles of the diffraction from each plane are indexed with respect to the XRD spectra. Hence we can conclude that the highly crystalline

anatase TiO$_2$ mesoporous layer was derived from the TiO$_2$ sol cured under ambient conditions.

### Temperature dependence of TiO$_2$ films

To evaluate the effect of temperature on the TiO$_2$ films developed from the sol, the films were subjected to various



**Fig. 3** FE-SEM surface morphology images of (a) 50 TiO$_2$, (b) 100 TiO$_2$, (c) 500 TiO$_2$, (d) MaPbI$_3$ film on 50 TiO$_2$, (e) MaPbI$_3$ film on 100 TiO$_2$ and (f) MaPbI$_3$ film on 500 TiO$_2$, and cross section image of MaPbI$_3$ film on (g) 50 TiO$_2$, (h) 100 TiO$_2$ and (i) 500 TiO$_2$.

annealing temperatures from 50 °C to 100 °C and 500 °C for 30 min, hereafter denoted as 50 TiO$_2$, 100 TiO$_2$, and 500 TiO$_2$. Fig. 2(a) shows the XRD spectra of TiO$_2$ annealed at various temperatures. The crystallinity of the films processed at 50 °C is in accordance with that of the 500 °C processed films; no significant change was observed from the XRD spectra. The absorbance (Fig. 2(b)) and transmission spectra (Fig. 2(b) inset image) also reveal identical properties for various annealing temperatures. It can be concluded that there is no notable change in the optical and crystallographic properties with a change in the temperature.

The variation in electrical properties with change in temperature, the direct current (DC) conductivity of the TiO$_2$ films sintered at various temperatures were analysed by studying the current–voltage characteristics of FTO/TiO$_2$/Au devices as shown in Fig. S2(a)–(c) (ESI†). The conductivities ($\sigma_0$) were measured using the formula $I = \sigma_0 A d^{-1} V$, where $A$ is the active area (0.12 cm$^2$) and $d$ (150 nm) is the thickness of the film.[21] The conductivity was measured from the ohmic contact region of the IV spectra plotted in log–log scale as the TiO$_2$ is a semiconductor material. 50 TiO$_2$ exhibited a conductivity of $1.6 \times 10^{-4}$ s cm$^{-1}$, 100 TiO$_2$-$1.8 \times 10^{-4}$ s cm$^{-1}$ and 500 TiO$_2$-$1.6 \times 10^{-4}$ s cm$^{-1}$. The conductivity values of the film exhibited only a minor change. To further verify the quality of the TiO$_2$ thin films, the trap density was calculated using the space charge limited current (SCLC) method (FTO/TiO$_2$/PCBM/Ag) (Fig. S2(d)–(f), ESI†). The trap state density was found to increase with an increase in temperature; the values increased from $6.37 \times 10^{17}$ cm$^{-3}$ for 50 TiO$_2$ to $6.97 \times 10^{17}$ cm$^{-3}$ for 100 TiO$_2$ and $7.12 \times 10^{17}$ cm$^{-3}$ for 500 TiO$_2$.

The effect of temperature on the surface properties of the TiO$_2$ films was analysed by evaluating the surface roughness of the films with the help of a contact profilometer. 50 TiO$_2$ exhibited an average roughness of 30.0 nm, 100 TiO$_2$ 35.1 nm and 500 TiO$_2$ 117 nm. The roughness of the 500 TiO$_2$ films was very high compared to the 50 and 100 TiO$_2$. The surface roughness of the ETL films is one of the critical factors determining the quality of the perovskite film that grows on it. To evaluate the effect of roughness on perovskite film growth, the surface morphology images of 50, 100 and 500 TiO$_2$ before (Fig. 3(a)–(c)) and after perovskite film deposition (Fig. 3(d)–(f)) were recorded. It can be observed that the perovskite films formed on 50 TiO$_2$ are free of pinholes and consist of well-interconnected perovskite grains. The perovskite films grown on 100 TiO$_2$ consist of pinholes, whereas those grown on 500 TiO$_2$ films show dendrite-like structures with many pinholes. Fig. 3(g)–(i) shows the cross section of perovskite films grown on TiO$_2$ films. Dense MaPbI$_3$ films were grown on 50 TiO$_2$. Likewise, the perovskite film on 100 TiO$_2$ is also dense, but the surface morphology shows pin holes. The



Fig. 4 Trap density and electron mobility calculations from IV spectra using the SCLC method for MaPbI$_3$ deposited on (a) 50 TiO$_2$, (b)100 TiO$_2$ and (c) 500. (d) Schematic diagram of the electron only device with device architecture TiO$_2$/MaPbI$_3$/PCBM/C.

Fig. 5   Contact angle measurements of (a) 50 TiO$_2$, (b) 100 TiO$_2$, and (c) 500 TiO$_2$.

MaPbI$_3$ film grown on 500 TiO$_2$ consists of large pin holes, which is quite evident from the cross-section and the surface image. Hence, it can be concluded that TiO$_2$ films with lower roughness aid the growth of high-quality perovskite films.

To ascertain the quality of the perovskite films formed on the TiO$_2$ sintered at various temperatures, SCLC was carried out by constructing an electron only device (TiO$_2$/MaPbI$_3$/PCBM/Ag). The trap densities and the electron mobility of the perovskite deposited on 50, 100, and 500 TiO$_2$ were calculated from the IV graphs (Fig. 4(a)–(c)), and Fig. 4(d) gives the schematic representation of the electron only devices fabricated for the analysis. Lower trap-filled limit voltage ($V_{TFL}$) is obtained for 50 TiO$_2$, indicating that the defect density has been cut down with respect to 100 and 500 TiO$_2$.[22] MAPbI$_3$ deposited on 50 TiO$_2$ exhibited a trap state density of $9.88 \times 10^{17}$ cm$^{-3}$ and mobility of 0.0124 cm$^2$ V$^{-1}$ S$^{-1}$ 100 TiO$_2$ exhibited trap state density of $2.01 \times 10^{18}$ cm$^{-3}$ and mobility of 0.0108 cm$^2$ V$^{-1}$ S$^{-1}$, and 500 TiO$_2$ exhibited a trap density of $4.08 \times 10^{18}$ cm$^{-3}$ with a mobility of $4.66 \times 10^{-3}$ cm$^2$ V$^{-1}$ S$^{-1}$.

Hence, we can conclude that the perovskite films formed on 500 TiO$_2$ consisted of higher trap states and possess a lower electron mobility when compared to 50 and 100 TiO$_2$.

To probe the underlying reasons for the poor quality perovskite films grown on 500 TiO$_2$, the surface energy of the TiO$_2$ films was studied using the contact angle measurement (Fig. 5(a)–(c)). The high surface energy of the TiO$_2$ surface is preferable for the wetting of the perovskite precursor.[21] At the solvent–substrate interface, three forces are exerted by the surface tensions at three interfaces: liquid–surface (ls), liquid–vapour (lv), and solid–vapour (sv). At equilibrium, the forces are balanced and can be written as $\gamma_{sv} = \gamma_{ls} + \gamma_{lv} \cos\theta$, where $\cos\theta$ gives the $x$-component of the liquid–vapour surface tension. Hence, $\cos\theta = \frac{\gamma_{sv} - \gamma_{ls}}{\gamma_{lv}}$ can be written. If $\gamma_{sv} > \gamma_{ls}$, $\cos\theta$ is positive, and $\theta$ is <90°, which suggests that the surface is of high energy. At smaller contact angle values of the film, the surface energy of the films is higher rendering a lower critical free energy for nucleation of perovskite on the TiO$_2$ films.



Fig. 6   (a)–(c) Ti2p XPS spectra and (d)–(f) O1s XPS spectra of 50 TiO$_2$, 100 TiO$_2$ and 500 TiO$_2$.

**Fig. 7** (a) IV characteristics of CPSCs with 50 $TiO_2$, 100 $TiO_2$ and 500 sintered $TiO_2$ as the ETL; (b) PL spectra and (c) TRPL spectra of $MaPbI_3$ films deposited on 50 $TiO_2$, 100 $TiO_2$ and 500 sintered $TiO_2$. (d) Mott–Schottky analysis at 1 kHz for the $TiO_2/MaPbI_3$ carbon heterojunction solar cell.

The contact angle measurements help in determining the hydrophobicity/hydrophilicity of the $TiO_2$ surface. A hydrophilic surface ensures a highly wettable surface, ensuring complete coverage of the perovskite film on the $TiO_2$.[21] The interface between the electrode and the precursor facilitates heterogeneous nucleation, which is governed by the contact angle. 50, 100 and 500 °C films exhibit hydrophilicity, with 50 °C having the highest surface energy,[21] which can be co-related with the high-quality perovskite films formed on 50 $TiO_2$.

Subsequently, the surface chemistry of the $TiO_2$ films processed at various temperatures was analyzed using XPS to probe the variation in Ti valence states as a function of change in processing temperature. Fig. 6(a)–(c) represents the Ti2p spectra and Fig. 6(d)–(f) represents the O1s spectra of 50 $TiO_2$, 100 $TiO_2$, and 500 $TiO_2$. 50 $TiO_2$ exhibits a doublet peak at

458 eV and 463.8 eV corresponding to $Ti2p_{3/2}$ and $Ti2p_{1/2}$, which can be ascribed to $Ti^{4+}$ in the $TiO_2$ crystal lattice, along with a shoulder peak at 460.2 eV, which can be ascribed to $Ti2p_{3/2}$, which corresponds to $Ti^{3+}$ in the crystal lattice indicating the oxygen vacancies.[23] Similar peaks were observed in 100 $TiO_2$ and 500 $TiO_2$ with slight displacement in the doublet peak towards the lower energy side of the spectra. The relative area of the $Ti^{3+}$ $[Ti^{3+}/(Ti^{3+} + Ti^{4+})]$ peaks was calculated for 50 $TiO_2$, 100 $TiO_2$ and 500 $TiO_2$, and it was observed that the lowest values were attained for 50 $TiO_2$, indicating reduced oxygen vacancy defects in 50 $TiO_2$ with respect to the other $TiO_2$ electrodes under discussion.[23] The same interpretation was applied to the O1s spectra, where the spectra were deconvoluted into three distinctive peaks where they can be ascribed to $O–Ti^{4+}$ and the oxygen-deficient $O–Ti^{3+}$ corresponding to 529.1 eV and 531.1 eV, respectively, while the –OH groups attached to $TiO_2$ were present at 532.6 eV. A slight shift in the peaks towards high energy was observed with a change in the sintering temperatures. Notably, the relative density of –OH groups present at 50 $TiO_2$ is higher than 100 $TiO_2$ and 500 $TiO_2$. The presence of –OH groups on the surface facilitates better interaction with the polar perovskite precursor, aiding improved wettability compared to 100 $TiO_2$ and 500 $TiO_2$. Also,

**Table 1** Solar cell parameters of CPSCs with 50 $TiO_2$, 100 $TiO_2$ and 500 sintered $TiO_2$ as the ETL

| Device id | $V_{OC}$ (V) | $J_{SC}$ (mA cm$^{-2}$) | FF (%) | $\eta$ (%) |
|---|---|---|---|---|
| 50 $TiO_2/MaPbI_3/C$ | 0.98 | 22.3 | 49.0 | 11.1 |
| 100 $TiO_2/MaPbI_3/C$ | 0.95 | 21.5 | 38.3 | 8.2 |
| 500 $TiO_2/MaPbI_3/C$ | 0.95 | 19.2 | 39.0 | 7.5 |

**Table 2** Fitted parameters of MaPbI$_3$ films deposited on 50 TiO$_2$, 100 TiO$_2$ and 500 sintered TiO$_2$

| Film | $\tau_1$ (ns) | $\tau_2$ (ns) | $\chi^2$ |
|---|---|---|---|
| 50 TiO$_2$/MaPbI$_3$ | 5.43 | 18.7 | 1.08 |
| 100 TiO$_2$/MaPbI$_3$ | 6.16 | 56.3 | 1.09 |
| 500 TiO$_2$/MaPbI$_3$ | 5.6 | 41.0 | 1.01 |

the lower oxygen vacancies facilitate better conductivity, which is in accordance with the conductivity measurement data.

### CPSC performance

CPSCs were fabricated with various TiO$_2$ sintering conditions. Fig. 7(a) shows the IV characteristics of the devices with the solar cell parameters tabulated in Table 1. 50 TiO$_2$ exhibited the highest performance of 11.1% with a current density of 22.5 mA cm$^{-2}$ and $V_{OC}$ of 0.98 V. The current density of other ETLs was found to decrease with an increase in the TiO$_2$ sintering temperature. This decrement can be attributed to the poor coverage of the perovskite film due to the reduced surface energy of the TiO$_2$ films. The series resistance of the devices increases with the sintering temperature of TiO$_2$, which can be directly correlated with the changes occurring at the TiO$_2$ electrode surface, as discussed in the above sections. Pinholes in the perovskite films, which can be observed from the FESEM images, can lead to considerable series resistance between the perovskite and carbon layer.[24] 50 TiO$_2$ exhibited a higher fill factor and a lower series resistance due to the compact perovskite layer formed on the TiO$_2$ and has a robust interface with the carbon layer, which can be observed from the CPSC device cross section image (Fig. S3, ESI†), facilitating efficient charge extraction. This clearly indicates that the entire solar cell performance is highly influenced by the properties of the ETL on which the perovskite absorber layer is coated.

The charge extraction properties were analysed with the aid of photoluminescence spectroscopy (PL) (Fig. 7(b)) and time resolved photoluminescence spectroscopy (TRPL) (Fig. 7(c)). MaPbI$_3$ films deposited on 50, 100, and 500 TiO$_2$ were excited at 540 nm, and the emission spectra were recorded. 50 TiO$_2$ exhibited a high PL quenching followed by 100 TiO$_2$ and 500 TiO$_2$, indicating a fast charge extraction at the TiO$_2$/MaPbI$_3$ interface. A bi-exponential fit was used to extract the electron lifetime from the TRPL spectra and is recorded in Table 2. $\tau_1$, the fast decay component, is attributed to the injection of free carriers in the perovskite layer to the charge collection material, while $\tau_2$ indicated the recombination of the free carriers in the radiative channel.[25] 50 TiO$_2$/MaPbI$_3$ exhibits a faster decay ($\tau_1$) when compared to MaPbI$_3$ on 100 and 500 TiO$_2$. A lower $\tau_2$ value was recorded for 50 TiO$_2$/MaPbI$_3$, indicating lower recombination resulting in less $V_{OC}$ losses.

To further understand the operation mechanism of the CPSCs with TiO$_2$ sintered at various temperatures, capacitance–voltage measurement was carried out on TiO$_2$/MaPbI$_3$ heterojunction solar cells. The built-in potential was calculated to be 1.12 V, 1.06 V, and 1.04 V, respectively, for 50 TiO$_2$, 100 TiO$_2$, and 500 TiO$_2$ (Fig. 7(d)) from the interception of the

linear regime with the x-axis of the Mott–Schottky plot in Fig. 7(d), which helps to suppress the back reaction of electrons from the TiO$_2$ film to the MaPbI$_3$ film efficiently.[26] 50 TiO$_2$ devices exhibited a larger built-in potential indicating a higher depletion width at the TiO$_2$/MaPbI$_3$ interface, successfully inhibiting the back reaction of electrons and preventing recombination, yielding a high functioning device compared to the 100 TiO$_2$ and 500 TiO$_2$.[26] The thickness of various layers of the devices was analysed from the device cross-sectional images of the CPSCs given in Fig. S3 (ESI†).

To validate the superiority of the low temperature curable TiO$_2$ sol, 50 TiO$_2$ was compared with high temperature sintered commercial TiO$_2$ (Fig. S4 and Table S1, ESI†). The device fabrication uses a simplified fabrication process with fewer fabrication steps with a single high temperature process compared to the general CPSC fabrication. The devices exhibited an enhancement in power conversion efficiency compared to the commercial TiO$_2$ with an improved open circuit voltage and fill factor due to better TiO$_2$ surface properties when compared to the commercial TiO$_2$ surface.

## Conclusion

A low temperature curable TiO$_2$ sol, compatible with various coating techniques was used as the ETL in the separator and HTM-free CPSCs and was found to give an efficiency of 11% which was greater than the devices with commercial TiO$_2$ as the ETL. The temperature dependence and changes in electrical, crystallographic, optical, and morphological properties were analysed. It was observed that the quality of the perovskite films is highly dependent on the surface energy and roughness of the TiO$_2$ layer on which it is coated. Further optimization of the device architecture can yield a high performing device with a lower energy payback period. Since the sol can be generated in larger quantities, is compatible with various coating techniques, and can be processed at temperatures as low as ambient temperature, it can be used for flexible solar cell applications and also large-scale deposition techniques.

## Conflicts of interest

There are no conflicts to declare.

## Acknowledgements

## References

1 H. S. Jung and N. G. Park, Perovskite solar cells: From materials to devices, *Small*, 2015, **11**(1), DOI: **10.1002/smll.201402767**.

2  A. Kojima, K. Teshima, Y. Shirai and T. Miyasaka, Organo-metal halide perovskites as visible-light sensitizers for photovoltaic cells, *J. Am. Chem. Soc.*, 2009, **131**(17), 6050–6051, DOI: **10.1021/ja809598r**.

3  P. Roy, N. Kumar Sinha, S. Tiwari and A. Khare, A review on perovskite solar cells: Evolution of architecture, fabrication techniques, commercialization issues and status, *Sol. Energy*, 2020, **198**, 665–688, DOI: **10.1016/j.solener.2020. 01.080**.

4  Z. Ku, Y. Rong, M. Xu, T. Liu and H. Han, Full printable processed mesoscopic $CH_3NH_3PbI_3/TiO_2$ heterojunction solar cells with carbon counter electrode, *Sci. Rep.*, 2013, **3**, 3132, DOI: **10.1038/srep03132**.

5  T. Liu, L. Liu, M. Hu, Y. Yang, L. Zhang, A. Mei and H. Han, Critical parameters in $TiO_2/ZrO_2$/Carbon-based mesoscopic perovskite solar cell, *J. Power Sources*, 2015, **293**, 533–538, DOI: **10.1016/j.jpowsour.2015.05.106**.

6  M. Shahiduzzaman, S. Visal, M. Kuniyoshi, T. Kaneko, S. Umezu, T. Katsumata, S. Iwamori, M. Kakihana, T. Taima, M. Isomura and K. Tomita, Low-Temperature-Processed Brookite-Based $TiO_2$ Heterophase Junction Enhances Performance of Planar Perovskite Solar Cells, *Nano Lett.*, 2019, **19**, 598–604, DOI: **10.1021/acs.nanolett. 8b04744**.

7  Z. Cao, C. Li, X. Deng, S. Wang, Y. Yuan, Y. Chen, Z. Wang, Y. Liu, L. Ding and F. Hao, Metal oxide alternatives for efficient electron transport in perovskite solar cells: Beyond $TiO_2$ and $SnO_2$, *J. Mater. Chem. A*, 2020, **8**, 19768–19787, DOI: **10.1039/d0ta07282f**.

8  H. Zhou, Y. Shi, K. Wang, Q. Dong, X. Bai, Y. Xing, Y. Du and T. Ma, Low-temperature processed and carbon-based $ZnO/CH_3NH_3PbI_3/C$ planar heterojunction perovskite solar cells, *J. Phys. Chem. C*, 2015, **119**, 4600–4605, DOI: **10.1021/jp512101d**.

9  F. Deng, X. Sun, X. Lv, Y. Li, S. Li, Y. Z. Zheng and X. Tao, All room-temperature processing efficient planar carbon-based perovskite solar cells, *J. Power Sources*, 2021, **489**, 229345, DOI: **10.1016/j.jpowsour.2020.229345**.

10  J. P. Correa Baena, L. Steier, W. Tress, M. Saliba, S. Neutzner, T. Matsui, F. Giordano, T. J. Jacobsson, A. R. Srimath Kandada, S. M. Zakeeruddin, A. Petrozza, A. Abate, M. K. Nazeeruddin, M. Grätzel and A. Hagfeldt, Highly efficient planar perovskite solar cells through band alignment engineering, *Energy Environ. Sci.*, 2015, **8**, 2928–2934, DOI: **10.1039/c5ee02608c**.

11  Y. Li, J. K. Cooper, W. Liu, C. M. Sutter-Fella, M. Amani, J. W. Beeman, A. Javey, J. W. Ager, Y. Liu, F. M. Toma and I. D. Sharp, Defective $TiO_2$ with high photoconductive gain for efficient and stable planar heterojunction perovskite solar cells, *Nat. Commun.*, 2016, **7**, 1–7, DOI: **10.1038/ ncomms12446**.

12  D. Yang, R. Yang, J. Zhang, Z. Yang, S. Liu and C. Li, High efficiency flexible perovskite solar cells using superior low temperature $TiO_2$, *Energy Environ. Sci.*, 2015, **8**, 3208–3214, DOI: **10.1039/c5ee02155c**.

13  P. S. C. Schulze, A. J. Bett, K. Winkler, A. Hinsch, S. Lee, S. Mastroianni, L. E. Mundt, M. Mundus, U. Würfel,

S. W. Glunz, M. Hermle and J. C. Goldschmidt, Novel Low-Temperature Process for Perovskite Solar Cells with a Mesoporous $TiO_2$ Scaffold, *ACS Appl. Mater. Interfaces*, 2017, **9**, 30567–30574, DOI: **10.1021/acsami.7b05718**.

14  B. Conings, L. Baeten, T. Jacobs, R. Dera, J. D'Haen, J. Manca and H. G. Boyen, An easy-to-fabricate low-temperature $TiO_2$ electron collection layer for high efficiency planar heterojunction perovskite solar cells, *APL Mater.*, 2014, **2**(8), 081505–081508, DOI: **10.1063/1. 4890245**.

15  D. Li, Y. Chen, P. Du, Z. Zhao, H. Zhao, Y. Ma and Z. Sun, An annealing-free anatase $TiO_2$ nanocrystal film as an electron collection layer in organic solar cells, *RSC Adv.*, 2015, **5**, 88973–88978, DOI: **10.1039/c5ra16932a**.

16  C. Yang, M. Yu, D. Chen, Y. Zhou, W. Wang, Y. Li, T. C. Lee and D. Yun, An annealing-free aqueous-processed anatase $TiO_2$ compact layer for efficient planar heterojunction perovskite solar cells, *Chem. Commun.*, 2017, **53**, 10882–10885, DOI: **10.1039/c7cc01104k**.

17  M. Guo, D. Shen, Y. Li, M. A. Akram and M. Wei, $TiO_2$ Mesocrystals Processed at Low Temperature as the Electron-Transport Material in Perovskite Solar Cells, *Chem-SusChem*, 2020, **13**, 5256–5263, DOI: **10.1002/cssc.2020 01486**.

18  B. Ding, S. Y. Huang, Q. Q. Chu, Y. Li, C. X. Li, C. J. Li and G. J. Yang, Low-temperature $SnO_2$-modified $TiO_2$ yields record efficiency for normal planar perovskite solar modules, *J. Mater. Chem. A*, 2018, **6**, 10233–10242, DOI: **10.1039/ c8ta01192c**.

19  T. Shi, S. Lin, M. Fang, D. Kong, Y. Yuan, Y. Gao, B. Yang, H. Han and C. Zhou, Low-temperature fabrication of carbon-electrode based, hole-conductor-free and meso-scopic perovskite solar cells with power conversion efficiency >12% and storage-stability >220 days, *Appl. Phys. Lett.*, 2020, **117**, 163501, DOI: **10.1063/5.0025442**.

20  Y. Yang, K. Ri, A. Mei, L. Liu, M. Hu, T. Liu, X. Li and H. Han, The size effect of $TiO_2$ nanoparticles on a printable mesoscopic perovskite solar cell, *J. Mater. Chem. A*, 2015, **3**, 9103–9107, DOI: **10.1039/c4ta07030e**.

21  M. S. You, J. H. Heo, J. K. Park, S. H. Moon, B. J. Park and S. H. Im, Low temperature solution processable $TiO_2$ nano-sol for electron transporting layer of flexible perovskite solar cells, *Sol. Energy Mater. Sol. Cells*, 2019, **194**, 1–6, DOI: **10.1016/j.solmat.2019.02.003**.

22  G. Liu, B. Yang, H. Chen, Y. Zhao, H. Xie, Y. Yuan, Y. Gao and C. Zhou, In situ surface modification of $TiO_2$ by $CaTiO_3$ to improve the UV stability and power conversion efficiency of perovskite solar cells, *Appl. Phys. Lett.*, 2019, **115**, 213501, DOI: **10.1063/1.5131300**.

23  S. Ranjan, R. Ranjan, A. Tyagi, K. S. Rana, A. Soni, H. K. Kodali, V. Dalal, A. Singh, A. Garg, K. S. Nalwa and R. K. Gupta, Low-Temperature Microwave Processed $TiO_2$ as an Electron Transport Layer for Enhanced Performance and Atmospheric Stability in Planar Perovskite Solar Cells, *ACS Appl. Energy Mater.*, 2022, **5**, 2679–2696, DOI: **10.1021/ acsaem.1c02675**.

24 A. Bahtiar, S. Rahmanita and Y. D. Inayatie, Pin-Hole Free Perovskite Film for Solar Cells Application Prepared by Controlled Two-Step Spin-Coating Method, *IOP Conf. Ser.: Mater. Sci. Eng.*, 2017, **196**, 012037, DOI: **10.1088/1757-899X/196/1/012037**.

25 J. Yin, J. Cao, X. He, S. Yuan, S. Sun, J. Li, N. Zheng and L. Lin, Improved stability of perovskite solar cells in ambient air by controlling the mesoporous layer, *J. Mater. Chem. A*, 2015, **3**, 16860–16866, DOI: **10.1039/c5ta02843d**.

26 F. Zhang, X. Yang, H. Wang, M. Cheng, J. Zhao and L. Sun, Structure engineering of hole-conductor free perovskite-based solar cells with low-temperature-processed commercial carbon paste as cathode, *ACS Appl. Mater. Interfaces*, 2014, **6**, 16140–16146, DOI: **10.1021/am504175x**.